UNIVERSITY OF LATVIA

Summary of Doctoral Thesis

Guna Doķe

RED AND NEAR INFRA-RED PERSISTENT LUMINESCENCE OF TRANSITION METAL ACTIVATED GERMANATE MATERIALS

Riga 2023

UNIVERSITY OF LATVIA
FACULTY OF PHYSICS, MATHEMATICS AND OPTOMETRY

UNIVERSITY OF LATVIA

Guna Doķe

RED AND NEAR INFRA-RED PERSISTENT LUMINESCENCE OF TRANSITION METAL ACTIVATED GERMANATE MATERIALS

SUMMARY OF DOCTORAL THESIS

For a doctoral degree in physics and astronomy
Subfield of solid state physics

Riga, 2023

The doctoral thesis was carried out at the Institute of Solid State Physics, University of Latvia from 2012 to 2023.

The doctoral thesis contains the introduction, four chapters, the theses, and reference list.

Form of the doctoral thesis: dissertation in Physics and Astronomy, subfield of solid state physics.

Supervisor: Prof. *Dr. phys.* Anatolijs Šarakovskis, Head of the laboratory and leading researcher of Laboratory of Spectroscopy at Institute of Solid State Physics, University of Latvia.

Reviewers:

1) *Dr. habil. phys.* Linards Skuja, University of Latvia;
2) *Dr. phys.* Pāvels Onufrijevs, Riga Technical University;
3) *Prof. PhD.* Marco Kirm, University of Tartu (Estonia).

The thesis will be defended at the public session Doctoral Committee of Physics, Astronomy and Mechanics, University of Latvia, at 15:00 on May 12, 2023, in the conference hall of the Institute of Solid State Physics of University of Latvia.

The thesis is available at the Library of the University of Latvia,
Kalpaka blvd. 4.

Chairman of the Doctoral Committee *Dr. habil. phys.* Linards Skuja

Secretary of the Doctoral Committee Sintija Siliņa

© University of Latvia, 2023
© Guna Doķe, 2023

ISBN 978-9934-18-962-3
ISBN 978-9934-18-963-0 (PDF)

ANNOTATION

Persistent luminescence or afterglow or long-lasting phosphorescence is a luminescence characterised by the emission of radiation lasting from a few seconds to several days after the excitation source is turned off. Most of the persistent luminescence materials have emission in the visible part of the spectrum, especially in green. Despite great potential in applications, there is a lack of research on red and near infra-red emitting persistent luminescence materials. Therefore, this work is dedicated to the synthesis and analysis of novel red and near infra-red emitting persistent phosphors $MgGeO_3$: Cr^{3+} and $Mg_2Si_{1-x}Ge_xO_4$: Mn (x = 0.0 – 1.0). In addition, the possibility of improving the persistent luminescence properties of already known and recognised persistent luminescence material $MgGeO_3$: Mn^{2+} through the synthesis in a reducing atmosphere has been studied.

All materials have been synthesised by the solid state synthesis method and investigated using X-ray diffraction, optical spectroscopy, electron paramagnetic resonance and thermally stimulated luminescence.

It is concluded that all three materials are excellent persistent phosphors, and the samples with the optimal doping level and host composition exhibit a detectable afterglow well over 10 hours after switching off the excitation source.

This work focuses on the trap properties and their impact on the persistent luminescence mechanism. It is concluded that there are several discrete trap levels in the case of $MgGeO_3$: Mn^{2+}, and the synthesis atmosphere does not significantly impact the nature of the shallow traps responsible for room temperature persistent luminescence. In the case of $MgGeO_3$: Cr^{3+}, a continuous trap distribution is present. In $Mg_2Si_{1-x}Ge_xO_4$: Mn materials, the presence of both types of traps, discrete and continuous, were detected. The $Mg_2Si_{1-x}Ge_xO_4$: Mn stands out with the rarely reported feature of different Mn luminescence centres responsible for photoluminescence and for persistent luminescence.

Summarising the results, conclusions are drawn about the mechanisms of persistent luminescence and trap properties of $MgGeO_3$: Mn^{2+}, $MgGeO_3$: Cr^{3+} and $Mg_2Si_{1-x}Ge_xO_4$: Mn materials and their potential applications.

Keywords: Persistent luminescence; transition metals; germanates; traps; thermally stimulated luminescence; electron paramagnetic resonance.

TABLE OF CONTENTS

INTRODUCTION

Motivation

Persistent luminescence (PersL) is a luminescence characterised by the emission of radiation from few seconds to several days after the excitation source has been switched off. PersL materials are used mainly for technologically trivial applications, such as luminescent paints, safety signs and decorations. At the same time, research and development of novel PersL materials and their application in medicine, military technology, anti-counterfeiting, etc., are underway.

Currently, most of the well-developed materials emit light in the visible (VIS) part of the spectrum, especially green, which is not optimal or usable for several applications, such as night vision surveillance, biomedical imaging, etc., where red and near infra-red (NIR) emission would be necessary. Still, there is relatively less research on materials with emission bands in the red and NIR regions. Additionally, these materials rarely are as efficient in the sense of intensity and longevity as their counterparts emitting green and blue light. Besides, it should be noted that most of the used PersL phosphors currently employ rare-earth (RE) element ions as activators. RE elements are relatively expensive; thus, their use increases overall production costs for PersL phosphors. Therefore, the common tendency in the development of a new generation of PersL materials is to avoid RE elements by substituting them with elements from the other groups, primary transition metals (TM).

For red and NIR emission, manganese and chromium ions are commonly suggested. As TM ions, manganese and chromium are strongly affected by the crystal field surrounding them and, when introduced into a properly chosen matrix, can provide red afterglow in the case of Mn^{2+} and NIR afterglow in the case of Cr^{3+}. On the other hand, germanate materials have attached widespread attention due to the high density of trapping levels, and there are many reports on excellent Mn^{2+} and Cr^{3+} activated germanate persistent luminescence materials; therefore, the aim of this work was set as follows.

The aim and main tasks of the work

The aim of this work is to **design new and improve already established transition metal doped red and near infra-red persistent luminescence materials.**

To achieve this goal, the following tasks were set:

- Synthesis of Mn^{2+} and Cr^{3+} activated germanate materials using solid state synthesis method;

- ► Characterisation of material structure using X-ray diffraction (XRD) and electron paramagnetic resonance (EPR) methods;
- ► Characterisation of the spectroscopic properties of prepared materials using optical spectroscopy methods such as photoluminescence (PL) spectra, decay kinetics, photoluminescence excitation (PLE) spectra, PersL spectra and kinetics measurements;
- ► Analysis of defects in the synthesised materials, including characterisation of the charge carrier trap properties: depth, distribution, density and stability, and identification of corresponding defects using thermally stimulated luminescence (TSL) and EPR experimental methods.

Contributions of the Author

Most of the samples have been synthesised by the Author. The Author measured all the PL and PLE spectra and kinetics at room temperature (RT), PersL spectra and kinetics, TSL glow curves and XRD patterns. The Author has performed all data analysis, calculations, and visualisation and is the corresponding author of all scientific publications directly related to the thesis.

MSc Aija Kalnina has assisted with the synthesis of the samples. PhD Guna Krieke has performed low-temperature decay kinetic measurements. Dr.phys. Andris Antuzevics has carried out all EPR measurements and their preliminary analysis.

Scientific novelty

Within the framework of the dissertation, new, previously not reported, red and NIR PersL phosphors $MgGeO_3$: Cr^{3+} and $Mg_2Si_{1-x}Ge_xO_4$: Mn (x = 0.0 - 1.0) have been successfully synthesised and analysed. An interpretation of the luminescence mechanisms in them has been provided. In addition, the possibility of improving the PersL properties of already known and recognised PersL material $MgGeO_3$: Mn^{2+} has been studied. To obtain optimal luminescence properties of these materials, methods such as finding the optimal concentration of activators, synthesis in different atmospheres, and modification of the host material composition have been used.

Most of the results presented in this work have been published in peer-reviewed scientific journals indexed in the international scientific database SCOPUS, as well as presented at international and local scientific conferences.

1. THEORETICAL BACKGROUND

1.1. Persistent luminescence

It is accepted that the PersL process involves three key steps: 1) ionisation, 2) trapping, and 3) detrapping. The first step of the PersL process consists of electron excitation and delocalisation. Normally, an electron at an excited state is still attached to its parent ion; it is localised. However, if sufficient energy is provided, the electron can reach the conduction band (CB), becoming mobile and delocalised. For oxide-based phosphors, there are three typical electron delocalisation mechanisms. The first is a straightforward band-to-band transition if the absorbed energy $E \geq E_g$ where E_g is band gap energy. The other two are so-called charge transfer (CT) transitions. In **Fig. 1.1.** CT1 stands for CT from oxygen ion in the valence band (VB) to activator ion creating charge transfer band (CTB). If CTB is close enough to CB, some electrons may cross over to CB. Further, CT2 stands for CT from the ground state of the activator ion to the CB; therefore, photo-oxidation of the activator ions occurs. In all three cases, if an electron is transferred to the CB, a hole is left behind. Delocalised charge carriers can move throughout the crystal; however, at some point, the localisation of charge carriers at appropriate defect sites will occur. In other words – electrons will be trapped by electron traps, and hole traps will trap holes.

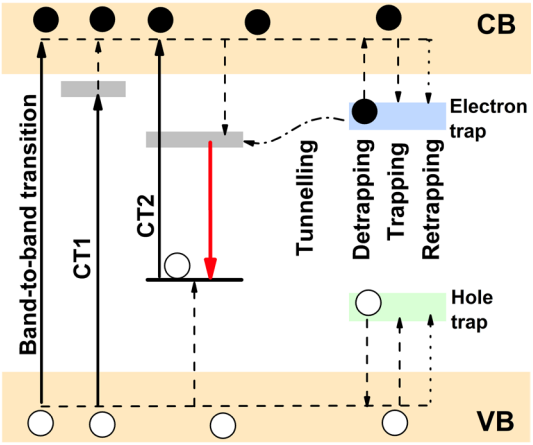

Fig. 1.1. Schematic diagram of the mechanism of PersL (● – electrons, ○ – holes).

After charge carriers have been trapped for some time, detrapping and consequent charge carrier recombination at the recombination centre occurs. There are two liberation possibilities – thermal promotion to CB or quantum tunnelling to the recombination centre. Additional competitive process – retrapping may occur. Retrapping is a process where the escaped charge carriers are recaptured before they reach recombination centres.

In general, decay of PersL intensity I in time t can be characterised with expression *Eq. (1.1)* where γ and l are fitting parameters, l usually is between 1 and 2; however, values as low as 0.5 has been reported [1,2]. When the tunnelling from an electron trap into a random distribution of recombination centres occurs, $l = 1$ or close to 1 [3,4].

$$I(t) = \frac{I_0}{(1+\gamma t)^l} \tag{1.1}$$

1.2. Point defects in crystals

The point defects expected in a real crystal can be divided into the following groups: vacancies – anion or cation is removed from its site and not replaced; interstitial – an ion, intrinsic or extrinsic, occupies an interstitial site that is normally empty; antisite – an ion on a site normally occupied by a different element which exists in the material; substitutional defects – an ion is substituted by an extrinsic ion and aggregate forms of the defects mentioned above [5].

Another subclass of defects is so-called colour centres, which are point defects or point defect aggregates associated with trapped electrons or holes. A typical example of a colour centre is F-centre. Here the presence of anion vacancy creates a localised positive charge since the negative ion which normally occupies the site is missing. If a free electron moves through the crystal, it will be attracted by the Coulomb force to the localised positive charge and can be trapped in the vacancy creating the F-centre. Analogous, a cation vacancy may be involved in a hole trapping; the system, in this case, is called the V-centre. Specifically, in oxides, by V-type centre, a hole trapped by oxygen and stabilised by a neighbouring cation vacancy is understood. There are several other colour centre types, such as M-centre (two neighbouring F-centres), V_k-centre (one hole shared by two adjacent anions), etc. Altogether it can be assumed that F-type centres serve as electron traps and V-type centres as hole traps.

In crystallography, if the dopant concentration extends 1%, it may be referred to as a solid solution rather than a doped material. However, most authors in the field of luminescence use term solid solution when describing a family of materials with a range of compositions and a single crystal structure.

A well-known example is NaCl – KCl solid solutions. NaCl and KCl have the same cubic crystal structure, and it is possible to make a pure compound with any ratio of Na^+ to K^+. Simply put, a solid solution is a crystalline phase with variable composition [6].

1.3. Properties of the transition metal ions

The TM elements are characterised by a partially filled d subshell and the ability to produce cations with an incomplete d subshell. As dopants in optical materials, mostly 3d elements are used [7].

Spectroscopically active orbitals in TM ions are also valence orbitals, leading to high environmental sensitivity. Consequently, different hosts will provide different optical properties of TM ion activators [8]. Namely, when the ion is a part of a crystal, the effect of the crystal field must be considered since it causes splitting and bending of the free ion energy levels. To determine the positions of energy levels of the TM ions in the crystal field, the Tanabe-Sugano diagrams for different d^n electron configurations are used [9].

2. LITERATURE REVIEW

2.1. Overview of persistent luminescence materials

There was no significant scientific interest in the PersL phenomenon until the 1990s. However, since then, the number of publications on the topic has rapidly grown.

The common host materials for PersL phosphors are oxides, silicates, aluminates, nitrides, germanates, gallates, etc. As dopants, typically, RE elements (e.g., Ce^{3+}, Eu^{2+}, Eu^{3+}, Tb^{3+}, Nd^{3+}, Pr^{3+}, Ho^{3+} Sm^{3+}, Tm^{3+}, Yb^{3+}, Dy^{3+}), TM ions (e.g., Cr^{3+}, Mn^{4+}, Mn^{2+}, Ni^{2+}, Fe^{3+}, Ti^{3+}) or post-transition group ions (e.g., Bi^{3+}, Pb^{2+}), are used.

There are established PersL phosphors for each of the primary colours, with the representative ones including Y_2O_2S: Eu^{3+}, Mg^{2+}, Ti^{4+} (red) [10], $SrAl_2O_4$:Eu^{2+}, Dy^{3+} (green) [11] and $CaAl_2O_4$:Eu^{2+}, Nd^{3+} (blue) [12]. However, compared to the blue and green emitting PersL materials, there are far fewer reports on red phosphors, with most of them still at the research and development stage, with unsatisfactory luminescence lifetime, intensity and other properties necessary for practical applications [13].

In addition to VIS emitting PersL phosphors, “invisible” UV and NIR emitters are also in demand. Because of their promising applications in biomedicine, interest in NIR PersL phosphors has rapidly increased over the last ten years. In turn, materials demonstrating long afterglow in UV are much less common, and publications on them have emerged in the last few years.

Right now, the best-known applications of PersL phosphors are somewhat trivial: “glow-in-the-dark” toys, luminous paints for decorations and watches, etc. Probably the most important and recognised commercialised application is safety signs in buildings and aeroplanes that persist to glow in the case of a complete lack of power [14]. In addition to these, a wide variety of other potential applications, such as bioimaging [15], road markings [16], fingerprint detection [17], and anti-counterfeiting [18], among others, have been suggested throughout the years.

There are several aspects to keep in mind when designing PersL phosphor. Firstly, choosing an optimal host and activator combination with desirable absorption and emission, suitable band gap, and appropriate traps is necessary. Secondly, an appropriate synthesis method and conditions must be chosen. In the case of solid state synthesis, a synthesis atmosphere may play a significant role, especially when working with oxygen rich hosts where oxygen vacancies typically serve as trapping centres, since synthesis in the reducing atmosphere or vacuum promotes their formation [19,20]. Lastly, there are several different routes to enhance the PersL properties of already known

materials. The commonly mentioned are co-doping, band gap engineering and persistent energy transfer.

2.2. Activators and hosts in this work

2.2.1. Persistent luminescence of Mn activated materials

Manganese is one of the most promising activators for red-emitting phosphors [21]. The Mn^{4+} ions tend to occupy highly symmetrical octahedral sites with relatively strong local crystal field and generates deep red emission with sharp peaks, typically in the 620 – 720 nm range [22]. On the other hand, Mn^{2+} may occupy both octahedral and tetrahedral sites, and the same $^4T_1(^4G) \rightarrow {}^6A_1(^6S)$ transition of Mn^{2+} can result in a widely different emission colour depending on molecular geometries in the material. The colour of Mn^{2+} emission in a strong field environment, such as an octahedral configuration, is red or even NIR [14]. In contrast, green emission appears in a weak field typically expected with a tetrahedral configuration. In all cases, broad featureless luminescence bands appear [23].

2.2.2. Persistent luminescence of Cr^{3+} activated materials

Cr^{3+} ions typically show intense luminescence ranging from 650 to 1200 nm, making Cr^{3+} the ideal luminescent centre for most red and NIR emitting materials [24]. If Cr^{3+} is in strong crystal field conditions, mainly spin forbidden $^2E(^2G) \rightarrow {}^4A_2(^4F)$ transition occurs, resulting in relatively narrow luminescence bands. On the other hand, when Cr^{3+} is in weak crystal field conditions, broadband luminescence is expected due to the spin allowed $^4T_2(^4F) \rightarrow {}^4A_2(^4F)$ transition. If an intermediate crystal field is present, there is thermal equilibrium between the $^2E(^2G)$ and $^4T_2(^4F)$ states and both narrow and broadband emissions of Cr^{3+} luminescence are observed [25].

2.2.3. $MgGeO_3$-based luminescent materials

The structure of $MgGeO_3$ is an analogue to Pbca enstatite. It consists of a three-dimensional network of $[GeO_4]$ tetrahedrons and two kinds of $[MgO_6]$ octahedrons: slightly distorted $[Mg(I)O_6]$ and more distorted $[Mg(II)O_6]$, which share joint edges. The schematic crystal structure and its basic units are presented in **Fig. 2.1**.

The first report on $MgGeO_3$ as a possible host for PersL phosphor was published in 2003 by Iwasaki *et al.* [26]. They discussed Mn doped $MgGeO_3$, Mg_2GeO_4 and Mg_4GeO_6. It was concluded that of the three, $MgGeO_3:Mn^{2+}$ has

the best PersL properties. The red afterglow ≈ 600 – 750 nm with a maximum of 680 nm was observed for at least an hour. Since then, this publication has given a base for various research projects about $MgGeO_3$: Mn^{2+} PersL materials [27,28].

Recently there have been reports on $MgGeO_3$: Mn^{2+} based materials that could be used for bioimaging and optical information storage applications. Possibly the most intriguing research comes from Zhang *et al.* 2020 publication [29], where they have designed PersL nanoparticles of $MgGeO_3$: Mn^{2+}, Yb^{3+}, Li^{+} with emission in the first and second biological windows that can be effectively used to realise long-term targeted imaging of inflammatory.

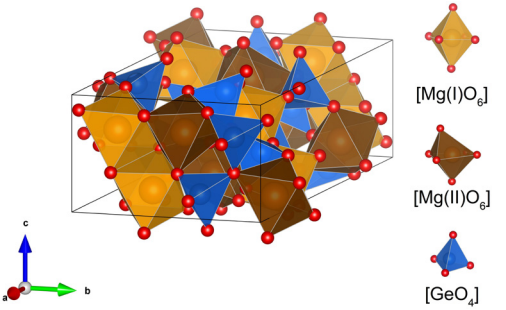

Fig. 2.1. Crystal structure of the $MgGeO_3$ material and polyhedron of Mg^{2+} and Ge^{4+}.

2.2.4. Mg_2GeO_4 and Mg_2SiO_4-based luminescent materials

The crystal structure of the Mg_2SiO_4 and Mg_2GeO_4 compounds is illustrated in **Fig. 2.2**. There are three types of polyhedrons present in each structure: $[GeO_4]$ or $[SiO_4]$ tetrahedrons and two distinct $[MgO_6]$ octahedrons. The two different cation octahedra form alternating chains parallel to the c axis. One of the octahedra is more distorted [30].

Just as $MgGeO_3$, Mg_2GeO_4 was first considered a possible host for PersL phosphor by Iwasaki *et al.* [26]. The material was doped by manganese, and Mn^{2+} characteristic PersL bands were observed. Nevertheless, up to now, there is only one other report on Mg_2GeO_4 based PersL phosphor [31].

On the other hand, Mg_2SiO_4 phosphors have drawn wide interest from the scientific community since the 1990s. However, almost all the publications concentrate on PL instead of PersL. The only report on PersL of Mn^{2+} doped Mg_2SiO_4 is the 2008 publication by Lin *et al.,* where they report on a long-lasting red phosphor: Mg_2SiO_4: Dy^{3+}, Mn^{2+} [32]. They observed two overlapping broad emission bands with maxima around 645 and 723 nm, which

were attributed to the transitions of Mn^{2+} ions substituting two non-equivalent Mg^{2+} sites.

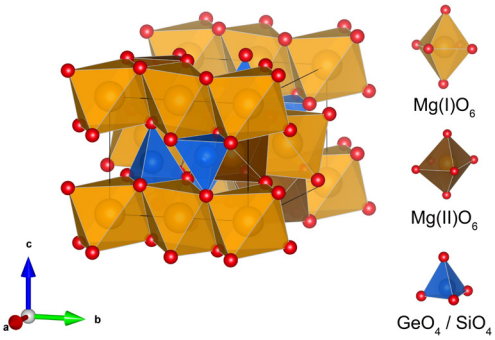

Fig. 2.2. Crystal structure of Mg_2SiO_4 and Mg_2GeO_4 and polyhedron of Mg^{2+}, Si^{4+} and Ge^{4+}.

3. EXPERIMENTAL

3.1. Synthesis and structure analysis of the samples

$MgGeO_3$: Mn^{2+}, $MgGeO_3$: Cr^{3+} and $Mg_2(Si_{1-x}Ge_x)O_4$: Mn samples were synthesised by a solid state synthesis method. During the synthesis, stoichiometric amounts of chemical compounds ($MgCO_3 \cdot Mg(OH)_2 \cdot 3H_2O$, GeO_2, SiO_2, MnO_2, Cr_2O_3) were weighted and milled in a marble mortar, transferred into a corundum crucible, and annealed:

- at 1250 °C for 2 h in either ambient or reducing (flux of N_2-H_2 mixture, 5% H_2) atmosphere to obtain polycrystalline $MgGeO_3$ materials doped with Mn^{2+};
- at 1250 °C for 2 h in an ambient atmosphere to obtain polycrystalline $MgGeO_3$ materials doped with Cr^{3+};
- at 1450 °C for 2 h in an ambient atmosphere to obtain polycrystalline $Mg_2(Si_{1-x}Ge_x)O_4$ materials doped with Mn.

A heating and cooling rate of 5 °C/min has been applied. After the synthesis, the samples were ground. For heat treatment, a high-temperature furnace Carbolite HTF18 was used.

The phase composition of prepared samples was studied with the powder XRD method. To obtain XRD patterns – the X-ray diffractometer Rigaku MiniFlex 600 was used. Positions of the XRD peaks were compared to the International Centre for Diffraction Data (ICDD) Powder Diffraction File (PDF) databases to identify the phase composition of the sample [33]. Additionally, the phase purity of synthesised materials was confirmed using Rietveld refinement performed using *Profex* software [34].

3.2. Analysis of the optical properties

To excite PL and PersL spectra in NIR and VIS spectral regions, a Nd: YAG Q-switched laser NT342/3UV (pulse duration – 4 ns) from Ekspla (wavelength tuneable from 210 nm to 2300 nm) was used as an excitation source. The spectra were recorded with either the Andor DU-490-A CCD camera in the case of NIR PL or the Andor iSTAR DH-734 CCD camera in the case of VIS PL. CCD cameras were coupled to Andor SR-303i-B monochromator/spectrometer.

To obtain PLE spectra, a Photoluminescence Spectrometer FLS1000 from Edinburgh Instruments was used. The excitation source of the system is a 450 W continuous xenon arc lamp. The PMT with spectral coverage from 200 nm to ≈ 870 nm was used for signal detection.

The isothermal PersL decay kinetics were measured using Lexsyg research fully automated TSL/OSL reader from Freiberg Instruments GmbH coupled with PMT Hamamatsu R13456 at 25 °C. As the irradiation source, a Q-switched short-pulsed UV laser DTL-389QT (wavelength 263 nm) from the Laser-compact Group was used.

All luminescence and excitation spectra measurements were corrected for the spectral sensitivity of the equipment.

3.3. Thermally stimulated luminescence

The TSL measurements were performed using previously mentioned Lexsyg research TSL/OSL reader. As the irradiation sources, a Q-switched short-pulsed UV laser DTL-389QT (wavelength 263 nm) from Laser-compact Group or X-ray tube VF-50 J/S, (40 kV, 0,5 mA, W-anode) were used.

A basic TSL glow curve may be used for the primary analysis of the trap properties. Firstly, the number of glow peaks represents the number of distinct traps in the material. Secondly, the position and intensity of each peak correspond to the trap depth and density of trapped charge carriers, respectively [35]. By applying more advanced measurement and analysis techniques, it is possible to evaluate the trap nature: whether there are discrete trapping sites or continuous distribution, as well as trap depth values, frequency factors, etc.

3.3.1. Evaluation of trap nature

$T_{max} - T_{stop}$, sometimes called partial thermal cleaning analysis, is a widely used experimental method for determining the number of glow peaks and their maximum temperature, which typically correlates with trap depth. Additionally, this method gives information about the nature of traps [36]. The basis of $T_{max} - T_{stop}$ is preheating previously irradiated sample to chosen tenperature T_{stop}, thereby thermally cleaning the glow curve up to that temperature. Following, the sample is cooled down to RT, and a TSL glow curve, as usual, is measured. The entire process, including irradiation, is repeated multiple times, each time, T_{stop} is increased by a few degrees. For each residual glow curve, the temperature corresponding to the first local maximum T_{max} is determined, and a plot of the T_{max} versus T_{stop} is made. If there is a single trapping site in the material, a straight line with a slope of 0 is expected. If the number of trapping sites is more than one, but they can be viewed as discrete traps, a “staircase” structure with each plateau region indicating the presence of an individual peak will appear. Finally, if the number of traps is high and they can be considered rather distributed than discrete, a straight line with a slope close to 1 is expected [37].

The method developed by Van den Eeckhout *et al*. [38] can be used to estimate trap depth density distribution. The premise of this method is a calculation of the difference between the integrated intensity of two consecutive TSL glow curves from the $T_{max} - T_{stop}$ experiment. Since integrated intensity is directly related to the total number of filled traps after the sample has been heated to the T_{stop}, the difference between the integrated intensities is a measure of the number of filled traps between the measurements. From this, the density of traps at different preheating temperatures can be acquired.

3.3.2. Evaluation of trap depth

For the evaluation of trap depths, two methods were used. First of which is various heating rate method [39]. It evaluates the shift of the glow peak position depending on the heating rate. From each measured glow curve, T_{max} of all glow peaks are noted. Using different heating rates β and *Eq. (3.1)*, one can obtain trap depth E_a for each peak.

$$\frac{\beta E_a}{k_B T_{max}^2} = s \cdot exp\left(\frac{E_a}{k_B T_{max}}\right). \tag{3.1}$$

Here k_B is the Boltzmann constant. The plot of $\left(\frac{1}{k_B T_{max}}\right)$ versus $\ln\left(\frac{T_{max}^2}{\beta}\right)$ should give a straight line with slope E_a.

The second is the Initial Rise Analysis (IRA). This method is based on analysing the initial low-temperature side of the TSL peak. It is assumed that the initial rise of the glow peak will follow the Arrhenius equation [40]:

$$I(T) = C \cdot \exp\left(-\frac{E_a}{k_B T}\right), \tag{3.2}$$

where I(T) – intensity as a function of temperature, C – a constant and T is a temperature. According to *Eq. (3.2)*, if ln(I) is plotted as a function of $\frac{1}{k_B T}$, a straight line with a slope $-E_a$ is obtained to represent the initial rise part of the glow peak.

3.4. Electron paramagnetic resonance

EPR spectra were measured with a Bruker ELEXSYS-II E500 CW-EPR spectrometer operated in the X (9.836 GHz) and Q (33.91 GHz) microwave frequency bands. The spectra acquisition parameters were: 10 mW microwave power and 0.2 mT magnetic field modulation amplitude. Stepwise sample

annealing was performed in a custom-built furnace in the air. For irradiation, an X-ray tube Spellman (40 kV, 20 mA, W anode) or a pulsed solid-state laser NT342/3UV from Ekspla was used. For EPR spectra simulations, the *EasySpin* software [41] was used.

EPR spectroscopy is based on the quantum physics notions of magnetic moment and spin of an electron. When an external magnetic field is applied, spin aligns either to or opposite the direction of the magnetic field, and the splitting of the electron spin sublevels occurs. This effect is referred to as the electron Zeeman splitting [42]. Energy difference hυ between splitted levels can be expressed by the following equation:

$$h\nu = g\mu_B B \tag{3.3}$$

where h – Planck's constant, υ – frequency of absorbed electromagnetic radiation, μ_B is a constant – the Bohr magneton, B – the strength of the applied magnetic field and g is the spectroscopic splitting factor, also called g-factor. g factor for free electron g_e is 2.0023 but varies significantly for paramagnetic ions in the solid state material.

In real crystal systems, in addition to interaction with the external magnetic field, other interactions may play a role in EPR spectra as well:

- electron-electron interaction in systems with multiple unpaired electrons appears in spectra as a "fine" structure;
- nucleus-electron interaction appears in spectra as a "hyperfine" structure;
- other interactions, such as the nuclear Zeeman interaction of the nuclear spins with the external magnetic field [43].

4. RESULTS AND DISCUSSION

4.1. Impact of synthesis atmosphere on $MgGeO_3:Mn^{2+}$

$MgGeO_3$: 0.1 mol% Mn^{2+} samples were synthesised in an ambient or a reducing atmosphere. Obtained samples will be denominated as aMGO and rMGO for ambient and reducing atmosphere synthesised materials, respectively.

XRD measurements confirmed that both samples can be characterised with a single-phase orthorhombic $MgGeO_3$ structure, corresponding to the PDF 00-034–0281. This suggests that manganese ions are well incorporated in the $MgGeO_3$ lattice. Based on the ionic radii, Mn^{2+} most likely occupies the Mg^{2+} sites.

Fig. 4.1. shows PLE (λ_{em} = 680 nm) and PL (λ_{ex} = 263 nm) spectra for both samples. Due to the relatively weak intensity of Mn^{2+} intra-atomic transition related excitation bands, the 340 – 450 nm spectral region of PLE is magnified. All observed excitation bands are in good accordance with multiple previous studies [27,44].

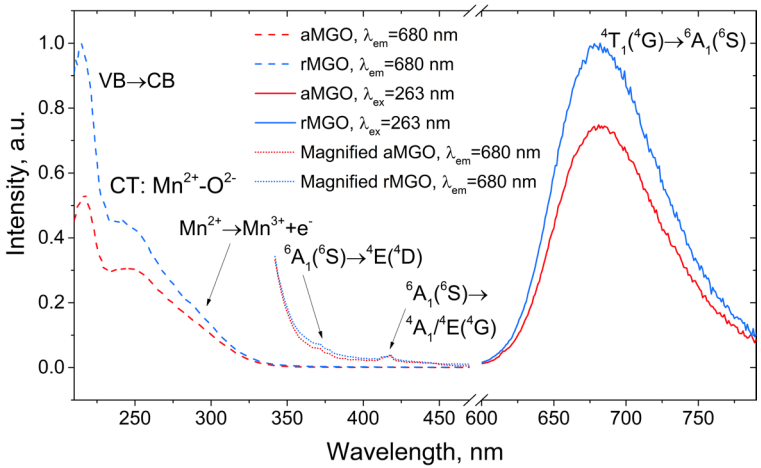

Fig. 4.1. The PLE (λ_{em} = 680 nm) spectra with magnified 340 – 450 nm part and PL (λ_{ex} = 263 nm) spectra of aMGO and rMGO.

For both samples, a strong red PL band between 600 – 800 nm with a maximum at 680 nm was observed when excited with UV. This band corresponds to Mn^{2+} optical transition from the excited state $^4T_1(^4G)$ to the

ground state $^6A_1(^6S)$ [45]. The synthesis in the reducing atmosphere slightly enhances the intensity of PL.

The excitation with UV leads to the creation of Mn^{2+} PersL in both samples. After irradiation with 263 nm for 3 min, PersL can be observed for more than 10 hours. The decay curves of PersL are shown in **Fig. 4.2.** For the first three hours rMGO sample have higher PersL intensity than the aMGO sample; after that, there is no significant difference. The decay profiles, when plotted in double-logarithmic plot, cannot be fitted with a single line; however, multiple linear parts with different slopes are visible for each curve. It is reasonable to expect complex decaying behaviours if various traps are involved in the generation of PersL. Therefore, decay profiles of the PersL of aMGO and rMGO samples indicate the presence of multiple types of traps.

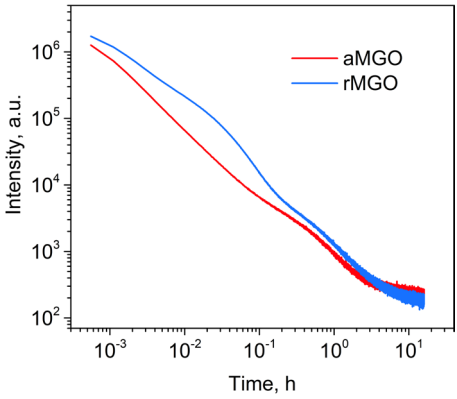

Fig. 4.2. The afterglow decay curves of the aMGO and rMGO samples. Irradiated for 3 min with 263 nm

To analyse the properties of the traps, TSL measurements were carried out, and the obtained glow curves are presented in **Fig. 4.3. (a).** Each glow curve consists of multiple peaks, with the most prominent glow peak around 125 °C. While in both cases glow peaks appear at the same temperature ranges, the synthesis in a reducing atmosphere promotes the relative intensity of glow peaks at lower temperatures indicating an increased relative density of shallow traps.

To determine a precise number of glow peaks, their maximum temperature and obtain information about the nature of traps, the $T_{max} - T_{stop}$ experimental method was applied. The obtained $T_{max} - T_{stop}$ plots are shown in **Fig. 4.3. (b,c)**. In the case of aMGO, there are five discrete traps in the temperature range from RT to 300 °C. Moreover, there are no substantial shifts

in T_{max} values which are approximately 53; 72; 122; 182; 276 °C, with changing T_{stop}. In the case of rMGO, the first four traps have slightly higher T_{max} values. However, they still are discrete traps by their nature. A significant difference between $T_{max} - T_{stop}$ plots of aMGO and rMGO samples appear in the high-temperature range where $T_{stop} > 200$ °C. The "staircase" shaped pattern in rMGO disappears, and data points can be easily fitted with a straight line. This strongly suggests that synthesis in a reducing atmosphere induces the appearance of a group of closely overlapping glow peaks related to continuous trap distribution [46].

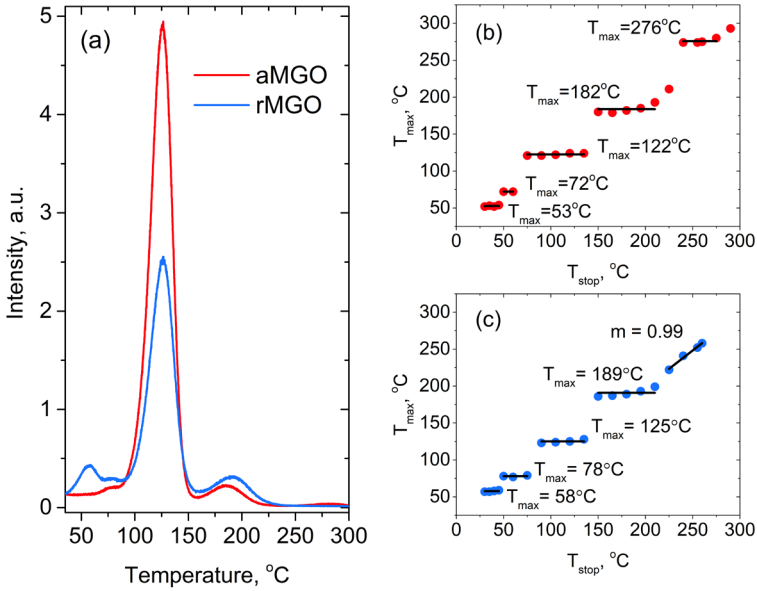

Fig. 4.3. (a) TSL glow curves of aMGO and rMGO samples irradiated with 263 nm; heating rate 1 °C/s. $T_{max} - T_{stop}$ plots for aMGO **(b)** and rMGO **(c)** samples.

Since it was shown in Ref. [47] that there are no significant differences in PL, PersL spectra and the glow peak positions between X-ray and UV irradiated samples, for convenience, further analysis was made for X-ray irradiated samples.

To evaluate E_a, the varying heating rate method was employed. Using different heating rates (0.25; 0.50; 1.00; 2.00; 4.00 °C/s) and *Eq. (3.1)*, trap depths corresponding to each peak were obtained. **Fig. 4.4.** shows sets of 5 points relevant to the specific glow peaks for both samples. Obtained trap depth values for aMGO sample are as follows: 0.60 ± 0.01 eV; 0.75 ± 0.02 eV; 0.91 ±

0.01 eV; 1.30 ± 0.04 eV; 1.55 ± 0.04 eV. And for the rMGO sample: 0.58 ± 0.02 eV; 0.73 ± 0.01 eV; 0.91 ± 0.02 eV; 1.30 ± 0.06 eV. Due to low signal intensity and interfering black-body radiation, the reliable activation energy range of continuously distributed traps in the high temperature end of glow curves of the rMGO sample could not be determined. However, this value is expected in the range around the activation energy corresponding to the deep trap of aMGO.

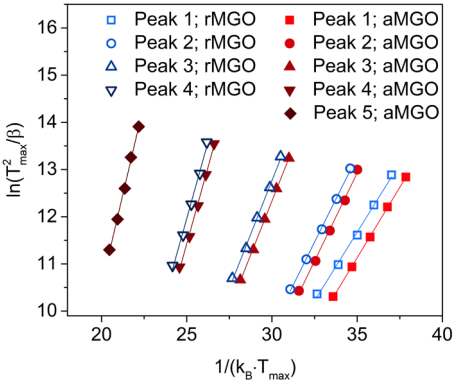

Fig. 4.4. Heating rate plots of rMGO and aMGO samples. The glow peaks have been labelled as Peak 1 to Peak 5 from the lowest to the highest T_{max}.

It has been reported that effective thermal promotion of electrons from traps to CB and, thus, excellent PersL performance at RT would be expected if the trap depths are up to 0.8 eV [48]. In the case of aMGO and rMGO, the first two trap depths fall into this range, and the energy of the most populated trap is 0.91 eV, which is quite close, leading to the long PersL of the material. The most significant difference in traps between aMGO and rMGO samples is observed in the case of deep traps, which give almost no contribution to PersL at RT.

EPR investigations before and after irradiation with X-rays were performed. The results for the rMGO sample are presented in **Fig. 4.5. (a).** After irradiation, a change in Mn^{2+} spectrum shape at 351 mT (g = 1.998). A mathematical spectra subtraction for the samples after and before irradiation reveals an additional component. The "Subtraction" signal was monitored for 8 h after irradiation. A negative shift from the free-electron *g* value suggests that the signal could belong to an F-type centre [49]. A likely candidate is an F^+ centre – one electron trapped in an oxygen vacancy. The characteristic decay time suggests a correlation between the observed EPR signal and the afterglow of the sample (**Fig. 4.5.(b)**). In a double-logarithmic representation, the EPR

signal change and the afterglow decay curve for the rMGO sample can be approximated as straight lines with similar slopes, which strongly indicates that the $g = 1.998$ EPR signal and decay of PersL are interrelated. The signal is unstable at RT; however, a complete recovery of the EPR spectrum to its initial form was observed only after annealing at 200 °C. Therefore, the experimental results suggest that the observed paramagnetic centre plays a role in thermally stimulated processes from RT up to 200 °C and could be associated with the first four glow peaks in the TSL glow curve.

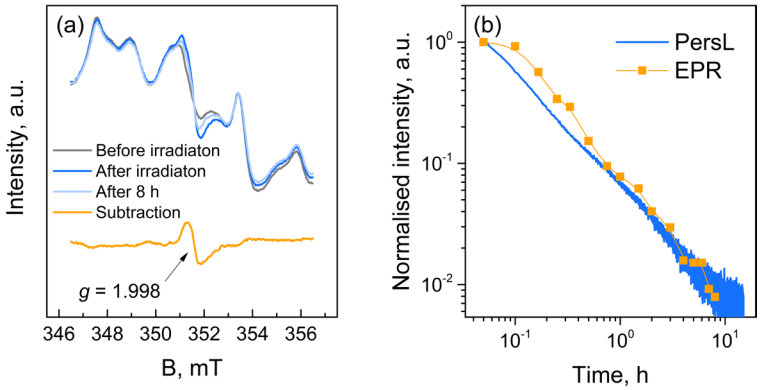

Fig. 4.5. (a) EPR spectra of rMGO sample before and after X-ray irradiation, **(b)** a comparison of g = 1.998 EPR signal decay and PersL decay curve after rMGO irradiation with X-rays.

4.2. NIR emission of $MgGeO_3$: Cr^{3+}

In pursuit of designing a novel broadband NIR PersL phosphor, a series of $MgGeO_3$: Cr^{3+} samples with varying concentrations of Cr^{3+} was synthesised. Obtained samples will be denominated as MGO, and concentration will be indicated with x where x = 0.10, 0.25, 0.50, 0.75, 1.00, 2.00 and 4.00 mol%.

XRD measurements confirmed that all samples can be characterised with a single-phase orthorhombic $MgGeO_3$ structure, corresponding to the PDF 00-034-0281. No disagreement in the XRD patterns for different doping concentrations was detected, suggesting that Cr^{3+} fully incorporates into the lattice of $MgGeO_3$ without any significant changes in the host matrix.

PLE and PL emission spectra are shown in **Fig. 4.6.** The excitation band at around 215 nm is assigned to the VB → CB transition of the host material, which is consistent with previously discussed aMGO and rMGO samples. The other three bands are attributed to the well-documented spin-allowed transitions

of Cr^{3+}: $^4A_2(^4F) \rightarrow {}^4T_2(^4F)$ in the case of 650 nm; $^4A_2(^4F) \rightarrow {}^4T_1(^4F)$ in the case of 453 nm and $^4A_2(^4F) \rightarrow {}^4T_1(^4P)$ in the case of 290 nm [50,51].

All samples exhibit a broadband emission in the NIR spectral region (around 700 – 1200 nm) when excited with UV radiation. It consists of multiple sub-bands, with the two most prominent bands having maxima at wavelengths around 790 nm and 980 nm. The origin of sub-bands is attributed to multiple non-equivalent positions for Cr^{3+} in the matrix.

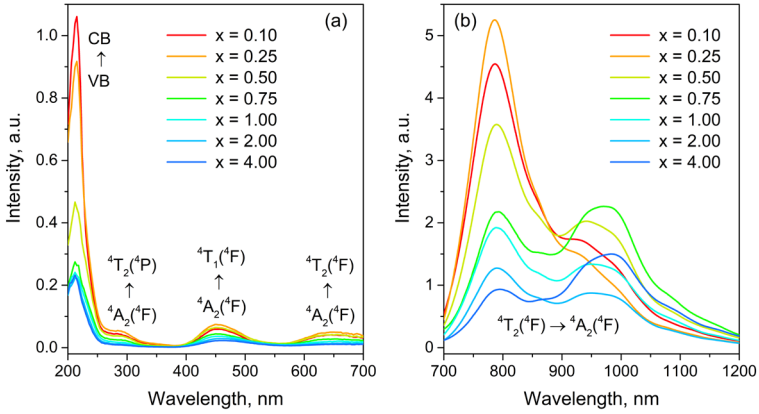

Fig. 4.6. (a) PLE spectra of the MGO samples monitored at 800 nm and **(b)** PL spectra excited with 263 nm.

After cessation of the UV excitation, an afterglow of the Cr^{3+} NIR luminescence band is easily detectable for more than 16 h. The PersL decay curves are shown in **Fig. 4.7**. The best PersL properties were detected for the sample doped with 0.25 mol% Cr^{3+}. PersL decay generally follows *Eq. (1.1)* and, in a double-logarithmic scale, appears as straight lines with slopes of $-l$. If the l value is close to 1, the mechanism of PersL is likely governed by tunnelling. In the case of MGO samples, regardless of the dopant concentration, the principal parts of the decay profiles are easily fitted with *Eq. (1.1)*, with l values oscillating between 0.95 and 1.03.

Detrapping through tunnelling does not require additional thermal energy; thereby, PersL should emerge in low-temperature conditions. As shown in the inset of **Fig. 4.7.**, MGO maintains its PersL phosphor properties at 150 K and even at 10 K temperatures.

To investigate the trap properties of the MGO materials, TSL and EPR measurements were performed. TSL glow curves of the MGO samples after irradiation with 263 nm are shown in **Fig. 4.8.(a).**

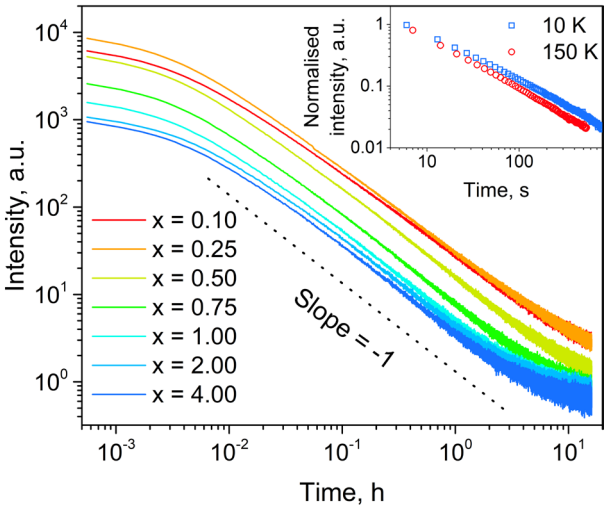

Fig. 4.7. The afterglow decay curves of the MGO samples after irradiation with 263 nm at RT for 10 min. Inset: the afterglow decay curves of the x = 0.25 mol% sample after irradiation with 263 nm at 10 K and 150 K.

There is no significant change in the structure and peak positions of the glow curves; however, the intensity of the peaks varies a lot. The sample doped with 0.25 mol% Cr^{3+} show the most significant potential, which is supported by the PersL decay measurements (**Fig. 4.7.**).

An extensive analysis of the x = 0.25 mol% Cr^{3+} sample was conducted to determine the nature of trap centres and depth. First, the $T_{max} - T_{stop}$ method was applied. The $T_{max} - T_{stop}$ plot is demonstrated in **Fig. 4.8.(b)** as grey squares. Up to T_{stop} = 100 – 120 °C, the T_{max} value is around 125 °C. The most likely explanation is that when T_{stop} is below a threshold value, the relatively deep traps present in MGO material are not significantly affected; thus, the peak of the glow curve does not change its position. When T_{stop} > 120 °C, T_{max} values increase linearly, suggesting continuously distributed or closely overlapping trapping levels.

The $T_{max} - T_{stop}$ measurements were used to determine the activation energy E_a as well. For this purpose, the IRA was used. The determined E_a values are shown as the orange circles in **Fig. 4.8. (b)**. E_a was found to be constant: 0.95 ± 0.05 eV. Similar results have been reported previously [52], and it has been suggested that in the case of a continuous trap distribution, IRA may predominantly give the E_a value of the shallower traps. Thus, it is concluded that relatively deep, closely overlapping trapping levels exist in the

MGO material. Analysing $T_{max} - T_{stop}$ glow curves, the trap density distribution of MGO material was found, it follows a Gaussian profile **Fig. 4.8. (c)**.

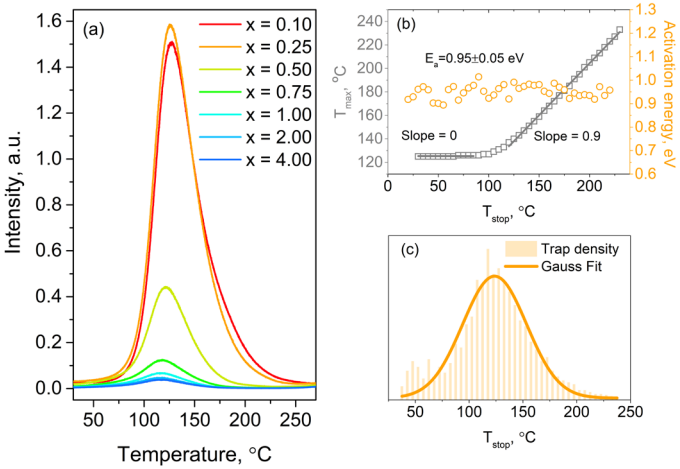

Fig. 4.8. (a) TSL glow curves of the MGO samples after irradiation with 263 nm; **(b)** $T_{max} - T_{stop}$ plot and E_a values; **(c)** the calculated trap density distribution.

EPR measurements before and after exposure to UV radiation were conducted; the results are shown in **Fig. 4.9. (a).** Complex EPR signals in 342 – 361 mT emerge after the irradiation.

EPR spectra simulations were performed to determine the UV-generated paramagnetic centres. The experimental spectrum was determined to be a superposition of signals of two S = ½ systems labelled "V-type" and "F-type". Here S is electron spin operator. The parameters used in simulations suggest the creation of single hole (V-type) and electron (F-type) centres in MGO. In oxide hosts, holes are commonly trapped on oxygen ions, forming S = ½ O^- centres. The detected centre in MGO exhibits a hyperfine structure likely linked to the ^{27}Al and ^{55}Mn isotopes. Both could be present as trace impurities from the precursors. From the detection of the hyperfine structure, it can be concluded that the holes are captured on oxygen ions with the respective impurity ions nearby. Common electron traps in oxides are oxygen vacancies. A single electron trapped at a vacant oxygen site, i.e., the F^+ centre is the most straightforward S = ½ F-type centre.

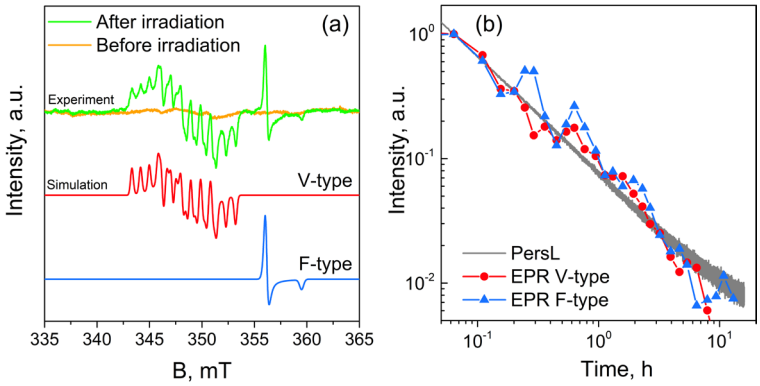

Fig. 4.9. (a) EPR spectra of the x = 0.10 mol% Cr^{3+} sample before and after UV irradiation; **(b)** EPR signal intensity decay compared to PersL decay kinetics.

At RT, the gradual decay of both paramagnetic centres is observed. Obtained results overlayed with PersL decay kinetics of the same sample are shown in **Fig. 4.9. (b)**. The analysis demonstrates that the decay rate of the paramagnetic centres is correlated with PersL kinetics. Therefore, the experimental evidence strongly suggests that the detected V-type and F-type centres in MGO play a crucial role in the mechanism of PersL.

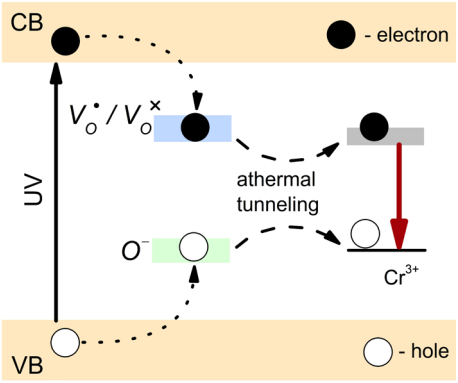

Fig. 4.10. A schematic diagram of the PersL mechanism in the MGO material.

Based on the results above, the primary mechanism of PersL in MGO is proposed in **Fig. 4.10**. Firstly, electrons are excited directly to the CB under UV irradiation, leaving holes in the VB. Charge carriers move through the

bands until they are captured by the traps. While the oxygen vacancies serve as the electron traps: $V_O^{\bullet\bullet} + e^- \rightarrow V_O^{\bullet}$ or $V_O^{\bullet\bullet} + 2e^- \rightarrow V_O^{\times}$, the holes are trapped on oxygen ions and form O^- centres: $O^{2-} + h^+ \rightarrow O^-$. When irradiation is stopped, charge carriers escape the traps by athermal tunnelling to Cr^{3+} ions. Finally, recombination at the Cr^{3+} ions occurs, resulting in long broadband NIR PersL.

4.3. Red emission of $Mg_2Si_{1-x}Ge_xO_4$: Mn

Here a design of manganese doped $Mg_2Si_{1-x}Ge_xO_4$ (x = 0.0 - 1.0) solid solutions are discussed in detail. A doping concentration of Mn is set at 0.1 mol%, and $Mg_2Si_{1-x}Ge_xO_4$: 0.1 mol% Mn (x = 0.0; 0.1; 0.2; 0.3; 0.4; 0.5; 0.6; 0.7; 0.8; 0.9; 1.0) materials will be denominated as MSGO with x values indicated where applicable.

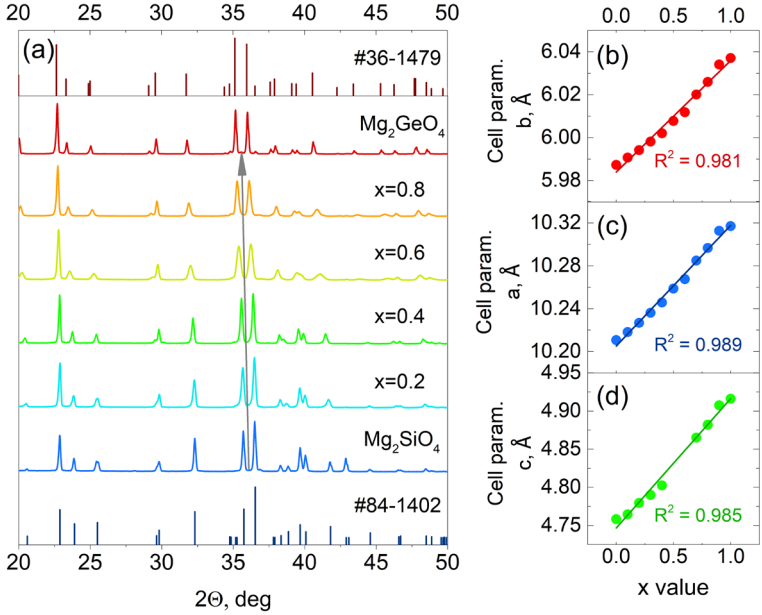

Fig. 4.11. (a) XRD patterns of selected MSGO samples and theoretical positions of Mg_2SiO_4 (PDF 01-084-1402) and Mg_2GeO_4 (PDF 00-036-1479); **(b,c,d)** dependence of the lattice parameters on x value.

Selected XRD patterns and standard cards PDF 01-084-1402 corresponding to orthorhombic Mg_2SiO_4 and PDF 00-036-1479 corresponding

to orthorhombic Mg_2GeO_4 are shown in **Fig. 4.11.(a).** The peak positions of the analysed samples matched well with the PDF patterns, and no additional phases could be identified, indicating the formation of $Mg_2Si_{1-x}Ge_xO_4$ solid solutions. The positions of the XRD peaks gradually shift to smaller angle values with the increase of Ge^{4+} content in the samples since relatively smaller Si^{4+} ions are replaced with larger Ge^{4+} ions, and subsequently, the interplanar distances increase. **Fig. 4.11.(b,c,d)** shows the dependence of the lattice parameters on the x value.

According to the ionic radii and the valence, Mn^{2+} ions most likely occupy both Mg^{2+} sites. Likewise, one could expect that Mn^{4+} ions would substitute Ge^{4+} ions. However, it has been demonstrated that Mn^{4+} ions strongly prefer an octahedral environment [53]. Thus, the most likely positions of Mn^{4+} in the lattice are $[MgO_6]$ octahedrons, where significant charge compensation would be necessary. Therefore, only a low concentration of Mn^{4+} is expected in MSGO samples.

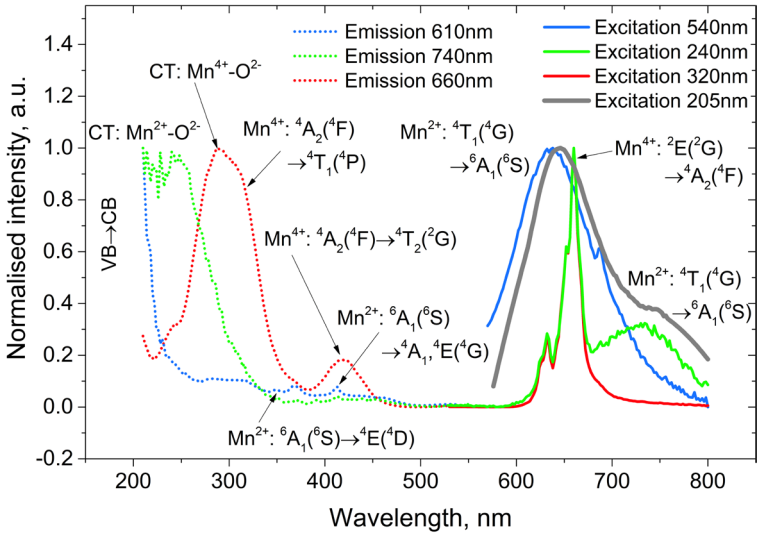

Fig. 4.12. PLE (λ_{em} = 610, 660, 740 nm) spectra and PL (λ_{ex} = 205, 240, 320, 540 nm) spectra of the x = 0.1 sample.

The luminescence measurements of MSGO reveal the coexistence of Mn^{2+} and Mn^{4+} in most of the samples. Selected PL and PLE spectra of the x = 0.1 sample are shown in **Fig. 4.12.** By varying the excitation wavelength, it is possible to observe three distinct PL bands: a sharp Mn^{4+} band with a maximum at 660 nm as a result of the $^2E(^2G) \rightarrow {}^4A_2(^4F)$ optical transition and

two broad Mn^{2+} bands with maxima at 637 and 730 nm corresponding to $^4T_1(^4G) \rightarrow {}^6A_1(^6S)$ optical transition of Mn^{2+} in two non-equivalent Mg^{2+} sites [54]. Excitation at 320 nm coincides with the spin-allowed Mn^{4+} intra-atomic transition from the ground state to $^4T_1(^4F)$ level; therefore, efficient Mn^{4+} PL even at minuscule doping concentration is not surprising.

When the sample is excited with 205 nm, corresponding to the VB → CB transition, a broadband PL emission matches a sum of both Mn^{2+} bands emerge. The same spectral features characterise the PersL spectra. All PLE bands, including CTBs and inter-atomic bands of Mn^{2+} and Mn^{4+} ions, correspond to previous reports on similar materials [32,55].

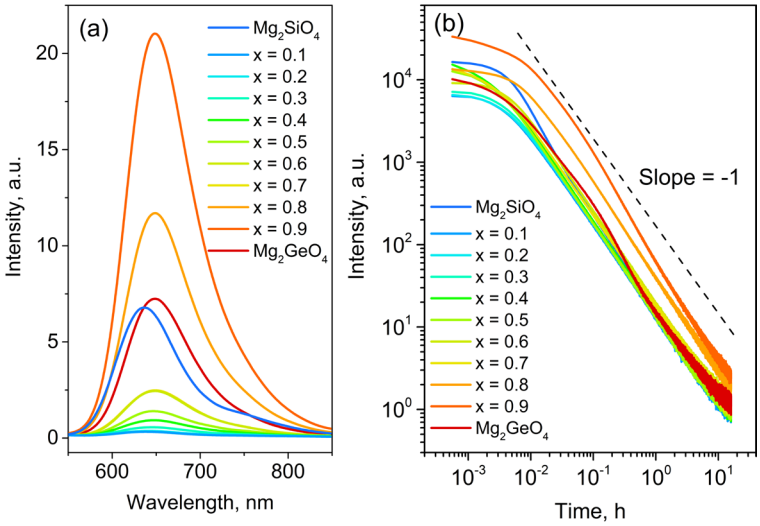

Fig. 4.13. (a) PersL spectra of the MSGO samples a few minutes after cessation of irradiation with 263 nm and **(b)** the afterglow decay curves of the same samples after irradiation for 3 min with 263 nm.

After removal of the 263 nm excitation, regardless of composition, all samples can be characterised with Mn^{2+} PersL (**Fig.4.13.(a)**). No detectable Mn^{4+} related PersL can be observed, thus, confirming the notion of low Mn^{4+} concentration in samples.

Based on the decay curves (**Fig.4.13.(b)**), it was concluded that the most perspective red PersL phosphor is the x = 0.9 sample. Afterglow could be easily detected for more than 16 h if samples were irradiated with a 263 nm. Most of the samples cannot be fitted with a single line, indicating the complexity of the PersL process with the involvement of multiple trap centres.

In addition, decay profiles do not follow the "-1" line; thus, although tunnelling cannot be entirely ruled out, it is doubtful that it plays a significant role in the RT PersL processes of MSGO materials. Even more, the coinciding of PersL spectra and PL spectra when excited with 205 nm strongly suggests that the PersL mechanism is based on thermal detrapping, i.e., trapped electrons are thermally promoted to CB before reaching the recombination centre.

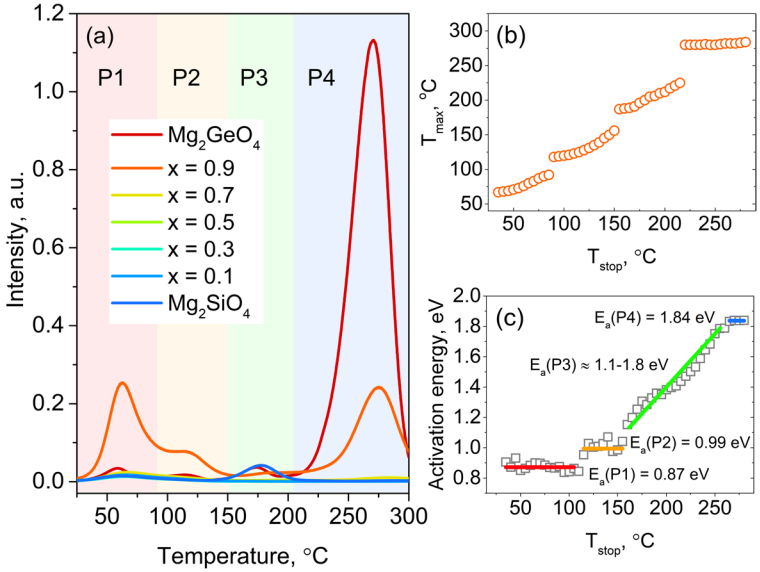

Fig. 4.14. (a) TSL glow curves of the MSGO samples after irradiation with 263 nm; **(b)** $T_{max} - T_{stop}$ plot; **(c)** $E_a - T_{stop}$ plot.

To study the trap properties of the MSGO materials, TSL glow curves were measured after irradiation with 263 nm. Selected glow curves are presented in **Fig. 4.14.(a)**. Multiple semi-overlapping glow peaks were detected throughout all measured temperature region; however, TSL glow curves can be roughly divided into four regions: P1 (25 – 90 °C), P2 (90 – 150 °C), P3 (150 – 210 °C) and P4 (210 – 300 °C). MSGO x = 0.9 sample has the highest intensity of shallow traps represented by peaks P1 and P2. This result is expected since this sample has been determined to be the best PersL phosphor of the set. Further examination was carried out for the x = 0.9 sample. The $T_{max} - T_{stop}$ experimental technique and IRA were applied. The $T_{max} - T_{stop}$ plot is shown in **Fig. 4.14. (b)**. Four distinct parts of the plot can be identified. By applying IRA, the trap depths E_a of the traps were determined (**Fig. 4.14. (c)**). The trap depth values corresponding to P1, P2 and P4 fluctuate around constant value

for each peak: E_a(P1) = 0.87 ± 0.01 eV, E_a(P2) = 0.99 ± 0.01 eV and E_a(P4) = 1.84 ± 0.01 eV. Thus, P1, P2 and P4 represent discrete trapping sites. Between P2 and P4 lies a relatively low-intensity glow curve region P3. The activation energy of the P3 increases with each increased T_{stop} and changes continuously from around 1.1 eV to 1.8 eV.

EPR spectroscopy analysis of UV-generated paramagnetic centres in the MSGO x = 0.9 sample is provided in **Fig. 4.15.(a).** The most notable features which emerge after the irradiation are a broad signal centred at ≈ 348 mT (g = 2.02) and a better-resolved signal at ≈ 352 mT (g = 1.99). EPR spectra simulations were carried out for more precise characterisation. The identified EPR signals in MSGO can likely be associated with single trapped hole O^- and single trapped electron F^+ centres [56].

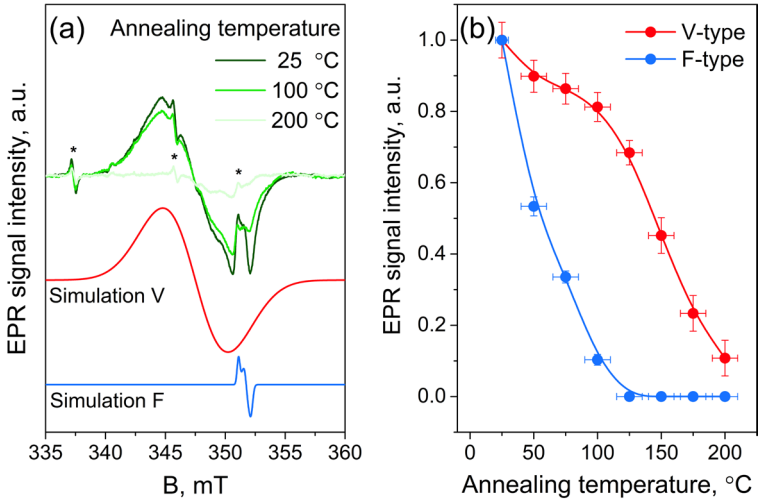

Fig. 4.15. (a) EPR spectra of undoped MSGO x = 0.9 sample after UV irradiation and subsequent annealing (trace impurity signals marked by the asterisks); **(b)** the decay of paramagnetic centres as a function of sample annealing temperature.

As evident from **Fig. 4.15.(b)**, the identified paramagnetic centres exhibit distinct annealing kinetics. The F-type centre decays rapidly in the 50 – 100 °C range. For the V-type centre, the annealing process can be divided into two stages: the first is correlated with the decay of the F-type centre, whereas the second extends up to 200 °C. Therefore, it can be concluded that the V-type centre has more than one complementary electron centre to recombine with.

Based on the obtained results, the primary mechanism of PersL in MSGO samples is proposed in **Fig. 4.16.** Under 263 nm irradiation, simultaneously, both Mn^{2+}-O^{2-} and Mn^{4+}-O^{2-} CTBs are excited. Due to the close distance between the bottom of CB and CTBs, some electrons from CTBs can be delocalized to the CB of the host via photoionization. From CB electrons are captured and trapped by the electron traps. At the same time, holes left in the VB will be trapped by hole traps. Once irradiation ceases, the trapped charge carriers can be released to the CB and VB by phonon assistance and transferred through the host to Mn^{2+}, where recombination takes place, resulting in red broadband PersL.

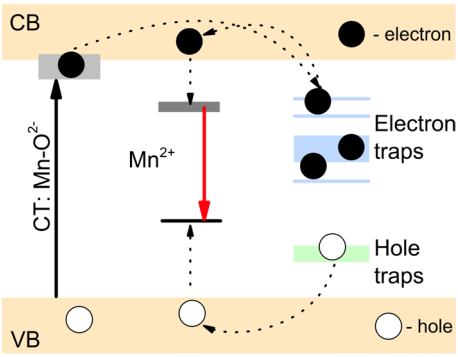

Fig. 4.16. A schematic diagram of the PersL mechanism in the MSGO material.

CONCLUSIONS

In conclusion, a novel broadband NIR PersL phosphor $MgGeO_3$, doped with various concentrations of Cr^{3+} and $Mg_2Si_{1-x}Ge_xO_4$: Mn, (x = 0.0 – 1.0) solid solutions doped with 0.1 mol% Mn were successfully synthesised by the solid state reaction. For both sets of samples, the optimal composition was determined. Additionally, $MgGeO_3$ material doped with 0.1 mol% Mn^{2+} was successfully synthesised by the solid state reaction in the reducing atmosphere for the first time.

For $MgGeO_3$: Mn^{2+} samples, regardless of the synthesis atmosphere, a strong red Mn^{2+} ($^4T_1(^4G) \rightarrow {}^6A_1(^6S)$) PL and PersL band with the maximum wavelength at 680 nm was observed. Synthesis in a reducing atmosphere slightly increases the luminescence intensity. After irradiation with 263 nm for 10 min, PersL was observed to last for at least 10 h for both samples. However, for the first few hours, the intensity of in reducing atmosphere synthesised sample is higher than that of in air synthesised sample. The observed PersL is a complex process involving multiple traps and is correlated with the decay of a $g = 1.998$ EPR signal, which appears after irradiation with X-rays.

TSL experiments determined that within the measured region sample synthesised in the air has five discrete traps with activation energies between 0.60 and 1.55 eV. In the case of the sample synthesised in reducing atmosphere, the first four traps have the same activation energies as the traps of the sample synthesised in air. Significant changes occur around the deepest trap energy range, where the synthesis in the reducing atmosphere promotes the appearance of closely overlapping trap levels. Additionally, the difference in the synthesis atmosphere impacts the distribution of filled traps in the material: synthesis in reducing atmosphere promotes an increase of shallow traps, thus, providing better PersL signal intensity.

In the case of $MgGeO_3$: Cr^{3+} samples, the broadband NIR PL and PersL attributed to the $^4T_2(^4F) \rightarrow {}^4A_2(^4F)$ optical transition of Cr^{3+} ions were observed. For the best performing sample with 0.25 mol% Cr^{3+}, the PersL signal was detected for more than 16 h after irradiation with 263 nm for 10 min.

Analysis of the TSL and EPR measurements has revealed that the main trap centres responsible for PersL are intrinsic by nature and can be categorised into two types: oxygen vacancies that serve as electron traps and oxygen ions that serve as hole traps. The traps in the material are deep and closely overlapping with $E_a \geq 0.9$ eV, and the trap density distribution closely follows the Gaussian profile. It was demonstrated that the primary detrapping mechanism in $MgGeO_3$: Cr^{3+} is athermal tunnelling directly to the luminescence centres. Therefore, the $MgGeO_3$: Cr^{3+} material is a promising NIR persistent phosphor not only at room and higher temperatures but also at low-temperature conditions, which may be beneficial for applications in

advanced fields such as anti-counterfeiting, night-vision surveillance, etc. Additionally, since the emission of $MgGeO_3$: Cr^{3+} covers the first and partially second biological windows, where low scattering and absorption of light guarantee deeper tissue penetration, a great potential for numerous biological applications for this material is evident.

Studies of $Mg_2Si_{1-x}Ge_xO_4$: Mn, (x = 0.0 – 1.0) solid solutions revealed that excitation with UV leads to appearance of red PL band with a maximum at 660 nm that originates from the $^2E(^2G) \rightarrow {}^4A_2(^4F)$ optical transition of Mn^{4+} ions. PersL can be induced in all the samples with the 263 nm excitation source. PersL emission consists of two broad bands with maxima at around 637 nm and 730 nm corresponding to $^4T_1(^4G) \rightarrow {}^6A_1(^6S)$ optical transitions of Mn^{2+} ions in two non-equivalent Mg^{2+} positions. The mixed valence of Mn ions present in the material and consequent dissimilar spectral features of PL and PersL spectra make the $Mg_2Si_{1-x}Ge_xO_4$: Mn materials a desirable candidate for advanced multimode anti-counterfeiting applications.

The best PersL phosphor of the series is $Mg_2Si_{0.1}Ge_{0.9}O_4$: Mn, for which red afterglow can be easily detectable for more than 16 hours after irradiation with 263 nm for 3 min.

The TSL analysis revealed a complex system of traps present in the material. Three distinct trap centres with trap depth values of 0.87 eV, 0.99 eV and 1.84 eV and a continuous distribution of closely overlapping trap levels with trap depth values around 1.1 – 1.8 eV were identified. The EPR analysis indicated the presence of two distinct paramagnetic centres associated with single trapped hole O^- and single trapped electron F^+ centres.

Optical measurements strongly suggest that PersL in $Mg_2Si_{1-x}Ge_xO_4$: Mn samples is realised through the classical “trap centre → CB → luminescence centre” model.

THESIS

- Synthesis of $MgGeO_3$: Mn^{2+} in reducing atmosphere not only improves the intensity of the afterglow signal by increasing the concentration of the shallow trapping centres, but also leads to the creation of continuous distribution of deep trapping centres in the material.

- Under the influence of UV radiation, deep, oxygen-related trapping centres are formed in $MgGeO_3$: Cr^{3+} material. Charge carriers from the from the trapping centres are transferred mainly by athermal tunnelling to the luminescence centre.

- The photoluminescence spectrum of $Mg_2Si_{1-x}Ge_xO_4$: Mn material, is dominated by characteristic signal of Mn^{4+} while the persistent luminescence spectrum is dominated by that of Mn^{2+}, which is explained by vastly different concentration and excitation efficiency of Mn^{2+} and Mn^{4+} ions in the material.

REFERENCES

[1] J. Trojan-Piegza, E. Zych, J. Hölsä, J. Niittykoski, Spectroscopic Properties of Persistent Luminescence Phosphors: Lu_2O_3: Tb^{3+}, M^{2+}(M = Ca, Sr, Ba), J. Phys. Chem. C. 113 (2009) 20493–20498. https://doi.org/10.1021/jp906127k.

[2] D. Kulesza, J. Trojan-Piegza, E. Zych, Lu_2O_3: Tb, Hf storage phosphor, Radiat. Meas. 45 (2010) 490–492. https://doi.org/10.1016/j.radmeas.2009.12.008.

[3] P. Avouris, T.N. Morgan, A tunneling model for the decay of luminescence in inorganic phosphors: The case of Zn_2SiO_4: Mn, J. Chem. Phys. 74 (1981) 4347–4355. https://doi.org/10.1063/1.441677.

[4] A. Vedda, M. Fasoli, Tunneling recombinations in scintillators, phosphors, and dosimeters, Radiat. Meas. 118 (2018) 86–97. https://doi.org/10.1016/j.radmeas.2018.08.003.

[5] H.L. Tuller, S.R. Bishop, Point defects in oxides: Tailoring materials through defect engineering, Annu. Rev. Mater. Res. 41 (2011) 369–398. https://doi.org/10.1146/annurev-matsci-062910-100442.

[6] R.C. Ropp, Solid State Chemistry, 2003.

[7] B. Di Bartolo, J. Collins, Handbook of Applied Solid State Spectroscopy, 2006

[8] T.E. Peters, R.G. Pappalardo, R.B. Hunt, Solid State Luminescence, Springer Netherlands, Dordrecht, 1993. https://doi.org/10.1007/978-94-011-1522-3.

[9] Y. Tanabe, S. Sugano, On the Absorption Spectra of Complex Ions II, J. Phys. Soc. Japan. 9 (1954) 766–779. https://doi.org/10.1143/JPSJ.9.766.

[10] X. Wang, Z. Zhang, Z. Tang, Y. Lin, Characterization and properties of a red and orange Y_2O_2S-based long afterglow phosphor, Mater. Chem. Phys. 80 (2003) 1–5. https://doi.org/10.1016/S0254-0584(02)00097-4.

[11] T. Matsuzawa, Y. Aoki, N. Takeuchi, Y. Murayama, A New Long Phosphorescent Phosphor with High Brightness, $SrAl_2O_4$: Eu^{2+}, Dy^{3+}, J. Electrochem. Soc. 143 (1996) 2670–2673. https://doi.org/10.1149/1.1837067.

[12] H. Yamamoto, T. Matsuzawa, Mechanism of long phosphorescence of $SrAl_2O_4$:Eu^{2+}, Dy^{3+} and $CaAl_2O_4$: Eu^{2+}, Nd^{3+}, J. Lumin. 72–74 (1997) 287–289. https://doi.org/10.1016/S0022-2313(97)00012-4.

[13] Y. Liu, B. Lei, Persistent Luminescent Materials, in: Phosphors, Up Convers. Nano Part. Quantum Dots Their Appl., Springer Singapore, Singapore, 2016: pp. 167–214. https://doi.org/10.1007/978-981-10-1590-8_6.

[14] R.E. Rojas-Hernandez, F. Rubio-Marcos, M.Á. Rodriguez, J.F. Fernandez, Long lasting phosphors: $SrAl_2O_4$: Eu, Dy as the most studied material, Renew. Sustain. Energy Rev. 81 (2018) 2759–2770. https://doi.org/10.1016/j.rser.2017.06.081.

[15] S. Wu, Y. Li, W. Ding, L. Xu, Y. Ma, L. Zhang, Recent Advances of Persistent Luminescence Nanoparticles in Bioapplications, Nano-Micro Lett. 12 (2020). https://doi.org/10.1007/s40820-020-0404-8.

[16] V. Castaing, E. Arroyo, A.I. Becerro, M. Ocaña, G. Lozano, H. Míguez, Persistent luminescent nanoparticles: Challenges and opportunities for a shimmering future, J. Appl. Phys. 130 (2021). https://doi.org/10.1063/5.0053283.

[17] D. Gao, F. Gao, Q. Kuang, X. Zhang, Z. Zhang, Y. Pan, R. Chai, H. Jiao, Zinc

Germanate Nanophosphors with Persistent Luminescence for Multi-Mode Imaging of Latent Fingerprints, ACS Appl. Nano Mater. (2022). https://doi.org/10.1021/acsanm.2c02163.

[18] B. Wang, Z. Wang, P. Mao, Y. Wang, A multi-color persistent luminescent phosphor b-$NaYF_4$: RE^{3+} (RE = Sm, Tb, Dy, Pr) for dynamic anti-counterfeiting, (2022). https://doi.org/10.1039/d2ra01425d.

[19] J. Trojan-Piegza, E. Zych, Afterglow luminescence of Lu_2O_3: Eu ceramics synthesized at different atmospheres, J. Phys. Chem. C. 114 (2010) 4215–4220. https://doi.org/10.1021/jp910126r.

[20] P. Liu, Y. Liu, C. Cui, L. Wang, J. Qiao, P. Huang, Q. Shi, Y. Tian, H. Jiang, J. Jiang, Enhanced luminescence and afterglow by heat-treatment in reducing atmosphere to synthesize the $Gd_3Al_2Ga_3O_{12}$: Ce^{3+} persistent phosphor for AC-LEDs, J. Alloys Compd. 731 (2018) 389–396. https://doi.org/10.1016/j.jallcom.2017.10.037.

[21] Q. Zhou, L. Dolgov, A.M. Srivastava, L. Zhou, Z. Wang, J. Shi, M.D. Dramićanin, M.G. Brik, M. Wu, Mn^{2+} and Mn^{4+} red phosphors: Synthesis, luminescence and applications in WLEDs. A review, J. Mater. Chem. C. 6 (2018) 2652–2671. https://doi.org/10.1039/c8tc00251g.

[22] L. Marciniak, K. Kniec, K. Elżbieciak-Piecka, K. Trejgis, J. Stefanska, M. Dramićanin, Luminescence thermometry with transition metal ions. A review, Coord. Chem. Rev. 469 (2022) 214671. https://doi.org/10.1016/j.ccr.2022.214671.

[23] M. Ayvacıkli, Z. Kotan, E. Ekdal, Y. Karabulut, A. Canimoglu, J. Garcia Guinea, A. Khatab, M. Henini, N. Can, Solid state synthesis of $SrAl_2O_4$: Mn^{2+} co-doped with Nd^{3+} phosphor and its optical properties, J. Lumin. 144 (2013) 128–132. https://doi.org/10.1016/j.jlumin.2013.06.040.

[24] G.N.A. De Guzman, M.-H. Fang, C.-H. Liang, Z. Bao, S.-F. Hu, R.-S. Liu, Near-infrared phosphors and their full potential: A review on practical applications and future perspectives, J. Lumin. 219 (2020) 116944. https://doi.org/10.1016/j.jlumin.2019.116944.

[25] M. Back, E. Trave, J. Ueda, S. Tanabe, Ratiometric optical thermometer based on dual near-infrared emission in Cr^{3+}-doped bismuth-based gallate host, Chem. Mater. 28 (2016) 8347–8356. https://doi.org/10.1021/acs.chemmater.6b03625.

[26] M. Iwasaki, D.N. Kim, K. Tanaka, T. Murata, K. Morinaga, Red phosphorescence properties of Mn ions in MgO–GeO_2 compounds, Sci. Technol. Adv. Mater. 4 (2003) 137–142. https://doi.org/10.1016/S1468-6996(03)00025-1.

[27] Y. Katayama, T. Kayumi, J. Ueda, S. Tanabe, Enhanced persistent red luminescence in Mn^{2+}-doped (Mg,Zn)GeO_3 by electron trap and conduction band engineering, Opt. Mater. (Amst). 79 (2018) 147–151. https://doi.org/10.1016/j.optmat.2018.03.033.

[28] X. Peng, Z. Tang, Y. Luo, L. Yang, M. He, X. Ye, Z. Zheng, X. Cui, C. Xia, F. Wang, Visual color modulation and luminescence mechanism studies on Mn/Eu co-doped Zn–Mg-Ge-O long afterglow system, Ceram. Int. 46 (2020) 14005–14018. https://doi.org/10.1016/j.ceramint.2020.02.200.

[29] S. Zheng, J. Shi, X. Fu, C. Wang, X. Sun, C. Chen, Y. Zhuang, X. Zou, Y. Li,

H. Zhang, X-ray recharged long afterglow luminescent nanoparticles $MgGeO_3$: Mn^{2+}, Yb^{3+}, Li^{+} in the first and second biological windows for long-term bioimaging, Nanoscale. 12 (2020) 14037–14046. https://doi.org/10.1039/C9NR10622G.

[30] A. Awad, A.F. Koster Van Groos, S. Guggenheim, Forsteritic olivine: Effect of crystallographic direction on dissolution kinetics, Geochim. Cosmochim. Acta. 64 (2000) 1765–1772. https://doi.org/10.1016/S0016-7037(99)00442-1.

[31] F. Xue, Y. Hu, L. Chen, H. Wu, G. Ju, T. Wang, L. Yang, A novel rare-earth free red long-persistent phosphor: Mg_2GeO_4: Mn^{4+}, Ceram. Int. 43 (2017) 15141–15145. https://doi.org/10.1016/j.ceramint.2017.08.044.

[32] L. Lin, M. Yin, C. Shi, W. Zhang, Luminescence properties of a new red long-lasting phosphor: Mg_2SiO_4: Dy^{3+}, Mn^{2+}, J. Alloys Compd. 455 (2008) 327–330. https://doi.org/10.1016/j.jallcom.2007.01.059.

[33] A. Bishnoi, S. Kumar, N. Joshi, Wide-Angle X-ray Diffraction (WXRD), in: Microsc. Methods Nanomater. Charact., Elsevier, 2017: pp. 313–337. https://doi.org/10.1016/B978-0-323-46141-2.00009-2.

[34] N. Doebelin, R. Kleeberg, Profex: A graphical user interface for the Rietveld refinement program BGMN, J. Appl. Crystallogr. 48 (2015) 1573–1580. https://doi.org/10.1107/S1600576715014685.

[35] A.J.J. Bos, Theory of thermoluminescence, Radiat. Meas. 41 (2006) S45–S56. https://doi.org/10.1016/j.radmeas.2007.01.003.

[36] S.W.S. McKeever, On the analysis of complex thermoluminescence. Glow-curves: Resolution into individual peaks, Phys. Status Solidi. 62 (1980) 331–340. https://doi.org/10.1002/pssa.2210620139.

[37] Y.S. Horowitz, D. Satinger, D. Yossian, M.E. Brandan, A.E. Buenfil, I. Gamboa-deBuen, M. Rodriguez-Villafuerte, C.G. Ruiz, Ionisation density effects in the thermoluminescence of TLD-100: Computerised T(m)-T(stop) glow curve analysis, Radiat. Prot. Dosimetry. 84 (1999) 239–242. https://doi.org/10.1093/oxfordjournals.rpd.a032727.

[38] K. Van den Eeckhout, A.J.J. Bos, D. Poelman, P.F. Smet, Revealing trap depth distributions in persistent phosphors, Phys. Rev. B. 87 (2013) 045126. https://doi.org/10.1103/PhysRevB.87.045126.

[39] M.S. Rasheedy, Method of Hoogenstraaten as a tool for obtaining the trap parameters of general-order thermoluminescence glow peaks, Radiat. Eff. Defects Solids. 160 (2005) 383–390. https://doi.org/10.1080/10420150500459999.

[40] Y. Zhang, R. Huang, Z. Lin, H. Li, D. Hou, J. Song, S. Lin, C. Song, H. Lin, Z. Lin, Positive effect of codoping Yb^{3+} on the super-long persistent luminescence of Cr^{3+}-doped zinc aluminum germanate, Ceram. Int. 44 (2018) 17377–17382. https://doi.org/10.1016/j.ceramint.2018.06.202.

[41] S. Stoll, A. Schweiger, EasySpin, a comprehensive software package for spectral simulation and analysis in EPR, J. Magn. Reson. 178 (2006) 42–55.

[42] B.J. Hales, Electron Paramagnetic Resonance (EPR) Spectroscopy, (2011) 1–16. https://doi.org/10.1002/9781119951438.eibc0310.

[43] C.F. De, O. Graeff, J. Niklas, R. Pandey, T. Biskup, Structure-Function Relationship of Organic Semiconductors: Detailed Insights From Time-Resolved EPR Spectroscopy, Front. Chem. 7 (2019).

https://doi.org/10.3389/fchem.2019.00010.
[44] A. Lecointre, A. Bessière, K.R. Priolkar, D. Gourier, G. Wallez, B. Viana, Role of manganese in red long-lasting phosphorescence of manganese-doped diopside for in vivo imaging, Mater. Res. Bull. 48 (2013) 1898–1905. https://doi.org/10.1016/j.materresbull.2013.01.017.
[45] J. Wang, S. Wang, Q. Su, Synthesis, photoluminescence and thermostimulated-luminescence properties of novel red long-lasting phosphorescent materials β-$Zn_3(PO_4)_2$: Mn^{2+}, M^{3+} (M = Al and Ga), J. Mater. Chem. 14 (2004) 2569–2574. https://doi.org/10.1039/b401685h.
[46] K. Brylew, W. Drozdowski, A.J. Wojtowicz, K. Kamada, A. Yoshikawa, Studies of low temperature thermoluminescence of GAGG:Ce and LuAG:Pr scintillator crystals using the T_{max}-T_{stop} method, J. Lumin. 154 (2014) 452–457. https://doi.org/10.1016/j.jlumin.2014.05.035.
[47] G. Doke, A. Antuzevics, G. Krieke, A. Kalnina, M. Springis, A. Sarakovskis, UV and X-ray excited red persistent luminescence in Mn^{2+} doped $MgGeO_3$ material synthesized in air and reducing atmosphere, J. Lumin. 234 (2021) 117995. https://doi.org/10.1016/j.jlumin.2021.117995.
[48] S.W.S. McKeever, Thermoluminescence of solids, 1983.
[49] A.S. Marfunin, Spectroscopy, luminescence and radiation centers in minerals, Springer Science & Business Media, 2012.
[50] N. Li, P. Zhang, Z. Wang, Z. Wei, Z. Jiang, Y. Shang, M. Zhang, Q. Qiang, L. Zhao, W. Chen, Novel UV and X-ray irradiated white-emitting persistent luminescence and traps distribution of $Ca_5Ga_6O_{14}$: Pr^{3+} phosphors, J. Alloys Compd. 858 (2021) 1–9. https://doi.org/10.1016/j.jallcom.2020.157719.
[51] X. Sun, L. Song, N. Liu, J. Shi, Y. Zhang, Chromium-Doped Zinc Gallate Near-Infrared Persistent Luminescence Nanoparticles in Autofluorescence-Free Biosensing and Bioimaging: A Review, ACS Appl. Nano Mater. 4 (2021) 6497–6514. https://doi.org/10.1021/acsanm.1c01115.
[52] P. Bolek, D. Kulesza, A.J.J. Bos, E. Zych, The role of Ti in charge carriers trapping in the red-emitting Lu_2O_3: Pr, Ti phosphor, J. Lumin. 194 (2018) 641–648. https://doi.org/10.1016/j.jlumin.2017.09.028.
[53] Y. Zhang, Y. Liu, L. Yang, S. Hu, Z. Wang, Z. Jing, H. Nian, B. Liu, G. Zhou, S. Wang, Preparation and luminescence properties of thermally stable Mn^{4+} doped spinel red-emitting ceramic phosphors, J. Lumin. 220 (2020) 117016. https://doi.org/10.1016/j.jlumin.2019.117016.
[54] L. Lin, M. Yin, C. Shi, W. Zhang, B. You, Synthesis and luminescence properties of red phosphors: Mn^{2+} doped $MgSiO_3$ and Mg_2SiO_4 prepared by sol-gel method, J. Rare Earths. 24 (2006) 104–107. https://doi.org/10.1016/S1002-0721(07)60334-2.
[55] H. Wu, Q. Zhu, X. Sun, J.-G. Li, Regulating anti-site defects in $MgGa_2O_4$:Mn^{4+} through Mg^{2+}/Ge^{4+} doping to greatly enhance broadband red emission for plant cultivation, J. Mater. Res. Technol. 13 (2021) 1–12. https://doi.org/10.1016/j.jmrt.2021.04.045.
[56] B. Henderson, J.E. Wertz, Defects in the alkaline earth oxides, Adv. Phys. 17 (1968) 749–855. https://doi.org/10.1080/00018736800101386.

LIST OF PUBLICATIONS

Publications reflecting the thesis

1. **G. Doke**, A. Antuzevics, G. Krieke, A. Kalnina, M. Springis, A. Sarakovskis, UV and X-ray excited red persistent luminescence in Mn^{2+} doped $MgGeO_3$ material synthesized in air and reducing atmosphere, J. Lumin. 234 (2021) 117995. https://doi.org/10.1016/j.jlumin.2021.117995.

2. **G. Doke**, A. Antuzevics, G. Krieke, A. Kalnina, A. Sarakovskis, Novel broadband near-infrared emitting long afterglow phosphor $MgGeO_3$: Cr^{3+}, J. Alloys Compd. 918 (2022) 165768. https://doi.org/10.1016/j.jallcom.2022.165768.

3. **G. Doke**, G. Krieke, A. Antuzevics, A. Sarakovskis, B. Berzina, Optical properties of red-emitting long afterglow phosphor $Mg_2Si_{1-x}Ge_xO_4$: Mn^{2+}/Mn^{4+}, Opt. Mater. (Amst). 137 (2023) 113500. https://doi.org/10.1016/j.optmat.2023.113500.

Other PersL related publications

1. A. Antuzevics, **G. Doke**, G. Krieke, P. Rodionovs, D. Nilova, J. Cirulis, A. Fedotovs, U. Rogulis, Shortwave Ultraviolet Persistent Luminescence of $Sr_2MgSi_2O_7$: Pr^{3+}, Materials (Basel). 16 (2023) 1776. https://doi.org/10.3390/ma16051776.
2. G. Krieke, **G. Doke**, A. Antuzevics, I. Pudza, A. Kuzmin, E. Welter, Tuneable persistent luminescence of novel $Mg_3Y_2Ge_3O_{12}$ garnet, J. Alloys Compd. 922 (2022) 166312. https://doi.org/10.1016/j.jallcom.2022.166312.
3. **G. Doke**, A. Kalnina, J. Cipa, M. Springis, A. Sarakovskis, Optical properties of near infrared persistent phosphor $CaZnGe_2O_6$: Cr^{3+}, M^{3+} (M^{3+} = B^{3+}; Al^{3+}; Ga^{3+}), Solid State Commun. 354 (2022) 114894. https://doi.org/10.1016/j.ssc.2022.114894.
4. A. Antuzevics, G. Krieke, **G. Doke**, B. Berzina, The origin of bright cyan persistent luminescence in Ca_2SnO_4:La^{3+}, Materialia. 21 (2022) 101374. https://doi.org/10.1016/j.mtla.2022.101374.

The Author of this dissertation is an author of 13 publications not related to PersL as well.

LIST OF INTERNATIONAL CONFERENCES AND SUMMER SCHOOLS

1. *iCOM&IWPPP 2022*, Belgrade, Serbia, August 29 – September 2, **G. Doke**, A. Antuzevics, G. Krieke, A. Sarakovskis, "Red and NIR persistent luminescence of magnesium germanate based materials", Book of abstracts, p. P-47.

2. *IWASOM 2022*, Gdańsk, Poland, July 10. – 15., 2022, **G. Doke**, G. Krieke, A. Antuzevics, B. Berzina, A. Sarakovskis, "Optical properties of red-emitting long afterglow phosphor $Mg_2Si_{1-x}Ge_xO_4$: Mn material", Book of abstracts, p. 95.

3. *FMNT&NIBS 2022*, Riga, Latvia, July 3. – 6., **G. Doke**, A. Antuzevics, G. Krieke, A. Kalnina, A. Sarakovskis "Novel broadband near-infrared emitting long afterglow phosphor $MgGeO_3$: Cr^{3+}", Book of abstracts, p. 137.

4. *DOC 2022*, Riga, Latvia, April 21. – 22., **G. Doke**, A. Kalnina, M. Springis, A. Sarakovskis "Optical properties of near infrared persistent phosphor $CaZnGe_2O_6$:Cr^{3+}, M^{3+} (M^{3+} = B^{3+}; Al^{3+}; Ga^{3+})", Book of abstracts, p. 56.

5. *DOC 2021*, Riga, Latvia, April 14.-16., **G. Doke**, G. Krieke, M. Springis, A. Sarakovskis „Near infrared long persistent luminescence of $CaZnGe_2O_6$:Cr^{3+} material" Book of abstracts, p. 22.

6. *DOC 2019*, Riga, Latvia, April 11.-12., **G. Doke**, G. Krieke, M. Springis, A. Sarakovskis, „Short-wave infra-red long persistent luminescence of $MgGeO_3$:Yb^{3+} material" Book of abstracts, p. 16.

Author of this dissertation has participated in 11 international and several local conferences with reports not related to PersL as well.

ACKNOWLEDGEMENTS

I want to express sincere gratitude to the scientific supervisor Professor *Dr. phys.* Anatolijs Sarakovskis, for the support and motivation throughout the years since the beginning of our cooperation in 2008.

I would also like to thank the collective of the Laboratory of Spectroscopy, especially *Dr. habil. phys.* Maris Springis, *Dr. phys.* Jurgis Grube, Professor *Dr. habil. phys.* Uldis Rogulis, *Dr. habil. phys.* Baiba Berzina, MSc. Aija Kalnina and MSc. Janis Cipa.

Special thanks to my closest colleagues, collaborators, motivators, listeners, comforters, encouragers, and game night adversaries, PhD Guna Krieke, *Dr.* Phys. Andris Antuzevics and (soon to be) PhD Meldra Kemere.

And without a doubt, the most immense gratitude to my family for their support and love. Especially to my parents Ilze and Gaidis, the partner in all sorts of crimes Martins and our little hurricanes Raimonds and Ernests.

Financial support provided from:

- "Strengthening of the capacity of doctoral studies at the University of Latvia within the framework of the new doctoral model", identification No. 8.2.2.0/20/I/006;
- The Latvian Council of Science project “Defect engineering of novel UV-C persistent phosphor materials” grant No. LZP-2021/1-0118;
- The Latvian Council of Science project “Novel persistent luminescent material – red light emitter” grant No. LZP-2019/1–0443;
- Scientific Research Project for Students and Young Researchers Nr. SJZS/2019/8;
- Scientific Research Project for Students and Young Researchers Nr. SJZ/2018/6;

is greatly acknowledged.

Institute of Solid State Physics, University of Latvia as the Center of Excellence has received funding from the European Union’s Horizon 2020 Framework Programme H2020-WIDESPREAD-01-2016-2017-TeamingPhase2 under grant agreement No. 739508, project CAMART²